HAL open science

Broadband coherent diffractive imaging

Julius Huijts, Sara Fernandez, David Gauthier, Maria Kholodtsova, Ahmed Maghraoui, Kadda Medjoubi, Andrea Somogyi, Willem Boutu, Hamed Merdji

To cite this version:

Julius Huijts, Sara Fernandez, David Gauthier, Maria Kholodtsova, Ahmed Maghraoui, et al.. Broadband coherent diffractive imaging. Nature Photonics, 2020, 14 (10), pp.618-622. 10.1038/s41566-020-0660-7 . cea-02959083

HAL Id: cea-02959083

https://cea.hal.science/cea-02959083v1

Submitted on 15 Feb 2024

HAL is a multi-disciplinary open access archive for the deposit and dissemination of scientific research documents, whether they are published or not. The documents may come from teaching and research institutions in France or abroad, or from public or private research centers.

L'archive ouverte pluridisciplinaire **HAL**, est destinée au dépôt et à la diffusion de documents scientifiques de niveau recherche, publiés ou non, émanant des établissements d'enseignement et de recherche français ou étrangers, des laboratoires publics ou privés.

ARTICLES
https://doi.org/10.1038/s41566-020-0660-7

nature photonics

Broadband coherent diffractive imaging

Julius Huijts[1], Sara Fernandez[1,3], David Gauthier[1,3], Maria Kholodtsova[1], Ahmed Maghraoui[1], Kadda Medjoubi[2], Andrea Somogyi[2], Willem Boutu[1] and Hamed Merdji[1]✉

Recent technological advances in attosecond science hold the promise of tracking electronic processes at the shortest space and time scales. However, the necessary imaging methods combining attosecond temporal resolution with nanometre spatial resolution are currently lacking. Regular coherent diffractive imaging, based on the diffraction of quasi-monochromatic illumination by a sample, is inherently incompatible with the extremely broad nature of attosecond spectra. Here, we present an approach that enables coherent diffractive imaging using broadband illumination. The method is based on a numerical monochromatization of the broadband diffraction pattern by the regularized inversion of a matrix that depends only on the spectrum of the diffracted radiation. Experimental validations using visible and hard X-ray radiation show the applicability of the method. Because of its generality and ease of implementation we expect this method to find widespread applications such as in petahertz electronics or attosecond nanomagnetism.

While in principle coherent imaging requires quasi-monochromatic radiation, its extension to broadband cases would open fascinating applications in attosecond science. Attosecond pulses that inherently exhibit broad spectra hold promise for tracking electron dynamics with ultimate details in both space and time[1–4]. So far, attosecond science has been restricted to spectroscopy studies even though real-space imaging has been envisioned. Table-top high-harmonic generation (HHG) sources can generate isolated attosecond pulses with a natural synchronization with the driving laser field that makes them suitable for pump–probe studies at the shortest timescales. Isolated attosecond pulses in the microjoule range[5], thus compatible with single-shot nanoscale imaging[6,7], are available in the vacuum ultraviolet (VUV) region. Recent advances are pushing HHG sources well into the soft X-ray regime, already covering the water window[8] and up to the kiloelectronvolt range[9] but with low photon output. Attosecond pulses at X-ray free-electron lasers are also emerging[4,10,11], promising orders of magnitude more peak power than table-top facilities.

Coherent diffractive imaging (CDI) is a powerful technique that has successfully validated single-shot femtosecond nanoscale imaging[6,7,12] after its first experimental demonstration[13]. By solving the so-called phase problem using a phase retrieval algorithm, CDI can be easily implemented. This lensless technique can reach a spatial resolution limited only by the wavelength and with the possibility to extend to three-dimensional (3D) perception[14–19]. However, CDI is based on the fundamental assumption of spatial and temporal coherence. Temporal coherence imposes the quasi-monochromaticity of the illumination. Its relevance to CDI can be explained from the Huygens–Fresnel principle: the scattered light from two points in a sample can no longer interfere if the difference in travel time to the detector is larger than the coherence time $\tau_c = \pi/\Delta\omega$, where $\Delta\omega$ is the angular frequency bandwidth of the illumination. For pulsed light sources, τ_c thus cannot exceed the pulse length. In general, for broadband sources (either of short pulses or continuous wave) the interference fringe visibility (the so-called speckle) decreases at the edges of the diffracted pattern, which restricts the useful numerical aperture of diffracted rays to low angles. This imposes a fundamental limit on the ultimate spatial resolution, Γ, given by $\Gamma = a\Delta\omega/\omega_c$, where a is the largest dimension of the object being imaged and ω_c is the central angular frequency of the source. In practice, CDI can tolerate a finite bandwidth to get a successful phase retrieval. For example, soft X-ray femtosecond pulses from HHG and VUV free-electron lasers hold reasonable bandwidths, around 0.5%, and still allow CDI convergence[6,7]. However, performing CDI with current attosecond pulses poses a real challenge due to their extremely broad spectra exceeding 10%. Novel strategies are required to solve the blurring of coherent diffractive patterns due to the broadband illumination and to allow for attosecond nanoscale imaging.

The first broadband phase-retrieval algorithm was introduced by Fienup to correct for aberration images from Hubble Telescope observations in the late 1990s[20]. Recent works have explored multiwavelength holographic imaging consistent with a train of attosecond pulses[21,22], two-pulse coherent imaging[23,24] or ptychography[25–27]. Other successful methods are an extension of the commonly used Gerchberg–Saxton algorithm[28] in parallel to the iterative phase retrieval process dubbed PolyCDI[29–33], showing convergence of up to 3.7% bandwidth. Here we present a method that allows for phase retrieval of a single broadband diffraction pattern, therefore being compatible with single-shot attosecond flash imaging. We first present the principle of the method, followed by two experimental validations using visible and hard X-ray radiation.

Results

Numerical monochromatization. In a CDI experiment, the scattered light from a sample is detected in the far field. The diffraction pattern from the Fraunhofer diffracted field at a distance z from the sample can be described as (see for example ref. [34]):

$$\Phi_\omega(x,y,z) = \left(\frac{\omega}{cz}\right)^2 \left|\psi_\omega\left(k_x = \frac{\omega}{cz}x, k_y = \frac{\omega}{cz}y, z = 0\right)\right|^2 \qquad (1)$$

where ω is the angular frequency of the illumination and $\psi_\omega(k_x, k_y, z = 0)$ denotes the 2D spatial Fourier transform of the field leaving the sample at $z = 0$, with k_x and k_y the spatial frequencies. Note that the far-field distribution shows a scaling factor ω/cz that is wavelength-dependent.

[1]LIDYL, CEA, CNRS, Université Paris-Saclay, CEA Saclay, Gif-sur-Yvette, France. [2]Synchrotron Soleil, Gif-sur-Yvette, France. [3]These authors contributed equally: Sara Fernandez, David Gauthier. ✉e-mail: hamed.merdji@cea.fr

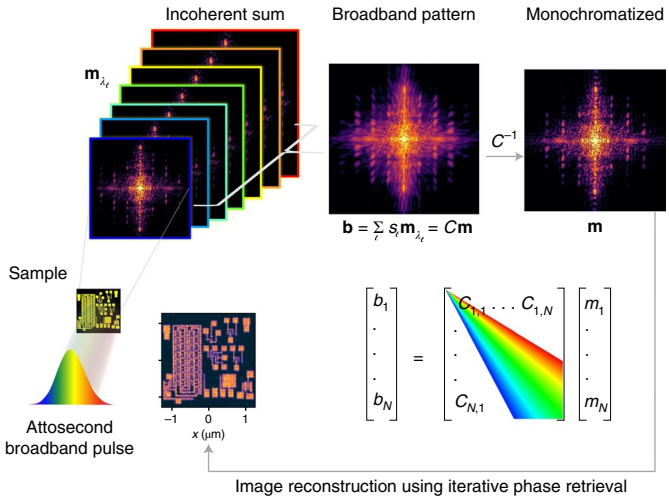

Fig. 1 | Principle of the numerical monochromatization. Conventional CDI assumes a monochromatic source. In the case of an attosecond broadband source, the diffraction pattern is the incoherent, spectrally weighted sum of the monochromatic diffraction patterns corresponding to all wavelengths present in the source. These monochromatic patterns are identical except for a geometric scaling. In the presented method this scaling is numerically inverted, thus yielding a monochromatized diffraction pattern. A conventional phase retrieval algorithm is then used to reconstruct the sample. The structure of the matrix C illustrates the method for the simplified case of a 1D diffraction pattern with the broadband and monochromatic patterns given by vectors $\mathbf{b}$ and $\mathbf{m}$, respectively. The monochromatization method consists in the inversion of the matrix–vector problem $\mathbf{b} = C\mathbf{m}$ in order to retrieve the monochromatic diffraction pattern from the broadband measurement. ℓ is the index that corresponds to the spectral discretization.

We will now assume that $\psi_\omega(k_x, k_y, z = 0) \approx s(\omega)\psi_{\omega_c}(k_x, k_y, z = 0)$, with $s(\omega)$ the spectrum of the diffracted radiation through the sample ($s(\omega) \in \mathbb{C}$, the set of complex numbers). We consider that the sample is spatially non-dispersive (s does not depend on the sample coordinates) over a given spectral range around the central frequency ω_c. This assumption is valid if the refractive indices of the materials in the sample do not change considerably over the spectrum of the source or if these changes are spatially homogeneous at the reconstructed length scales. Note that this assumption is also made in previous studies[29–33]. We can then express the diffraction pattern for a single angular frequency component:

$$\Phi_\omega(x, y, z) = \omega^2 S(\omega) M_{\omega_c}\left(\frac{\omega}{cz}x, \frac{\omega}{cz}y\right), \tag{2}$$

with $S(\omega)$ the power spectrum and M_{ω_c} the monochromatic diffraction pattern. Because the detector has an integration time much longer than the coherence time of the illumination, the broadband diffraction pattern is the incoherent sum of all angular frequency components, written as:

$$B(x, y, z) = \int \omega^2 S(\omega) M_{\omega_c}\left(\frac{\omega}{cz}x, \frac{\omega}{cz}y\right) \mathrm{d}\omega \tag{3}$$

with the integral taken over the whole spectrum. The measured broadband diffraction pattern B is thus given by the sum of scaled copies of the monochromatic diffraction pattern M_{ω_c}, weighted by the normalized spectral density $S(\omega)$, such that $\int \omega^2 S(\omega)\mathrm{d}\omega = 1$. This is schematically shown in Fig. 1. Note that the method depends only on the power spectrum of the scattered light.

In a conventional CDI experiment, the sample is reconstructed by the use of an iterative phase retrieval algorithm, which iterates between the monochromatic measured diffraction pattern and some constraints on the sample plane—typically the isolation of the object in real space—to converge to the solution. In our broadband case, a step of numerical monochromatization is introduced before the iterative process. By measuring the broadband diffraction pattern B and the spectrum of the diffracted radiation S, the retrieval of the monochromatic pattern M_{ω_c} is reduced to a linear algebra problem. Writing the monochromatic pattern as vector $\mathbf{m}$, the broadband pattern as vector $\mathbf{b}$ and the scaling matrix as C, the broadband diffraction can be simply written as:

$$\mathbf{b} = C\mathbf{m}. \tag{4}$$

The matrix C can be regarded as containing the radially dependent point-spread function of the convolution in equation (3). It maps a point in $\mathbf{m}$ to the shape of the spectrum in $\mathbf{b}$. This is schematically shown in Fig. 1. For a 2D diffraction pattern C becomes a 4D tensor, although in the numerical implementation the diffraction patterns are rearranged in a 1D vector, so that C is kept 2D.

The monochromatization of a broadband diffraction pattern is now reduced to the inversion of matrix C. The matrix C is invertible as the determinant is non-zero. This is only the case for a spectrum that does not contain any zeros. Although C is invertible, the problem is ill-conditioned. This means that the inversion is very sensitive to noise, either experimental or coming from the discretization. To mitigate this problem, a regularization method known as conjugate gradient least squares (CGLS)[35] is used (for details on the numerical implementation the reader is referred to the Methods, Extended Data Fig. 1 and ref. [36]).

In the present method, equation (3) is thus deconvolved in a standalone step, which depends solely on the spectrum of the diffracted radiation. It can be used with standard phase retrieval algorithms, as shown here, or integrated as a module in algorithms for other types of lensless imaging (holography, ptychography) to allow them to cope with broadband sources. Extensive simulations have been performed in ref. [36] on the method's applicability to ptychography.

Experimental validation. The monochromatization method was first validated in the visible domain on a broadband and spatially coherent source, and then using synchrotron hard X-ray radiation. The samples employed for these experiments are ubiquitous in the field of diffractive imaging and allow for algorithmic validation and resolution estimation.

Visible-light experiment. A scanning electron microscope (SEM) image of the sample is shown in Fig. 2e. The sample consists of a gold-coated silicon nitride membrane in which features emulating the number '70' were etched. The experiment was performed using laser pulses from an Yb:KGW femtosecond oscillator (1 W, 240 fs) focused into a photonic crystal fibre to generate a supercontinuum. After filtering the residual 1,030-nm pump light, the resulting broadband spectrum with a bandwidth $\Delta\lambda/\lambda = 11\%$ ($\lambda = 2\pi c/\omega$, where λ is the wavelength and c is the speed of light) is shown in Fig. 2a. For the narrowband case ($\Delta\lambda/\lambda = 1.2\%$), a 10-nm bandpass filter at 800 nm was used (Fig. 2a). The light scattered from the object was recorded by a charge-coupled device (CCD) camera set at 16 mm from the sample. Further details on the experimental set-up can be found in the Methods. When the sample is illuminated using narrowband radiation, the recorded diffraction patterns exhibit the expected coherent behaviour: size-modulated streaks arising from the upper lines of the '70' and concentric rings corresponding to the '0' shape dominate the pattern (Fig. 2b). By contrast, using the source's full broadband spectrum yields a diffraction pattern that blurs the coherent modulations (Fig. 2c), as described in equation (3) and mentioned in Fig. 1.

Our monochromatization method was then applied to the broadband pattern, at the centre of mass of the broadband spectrum, that

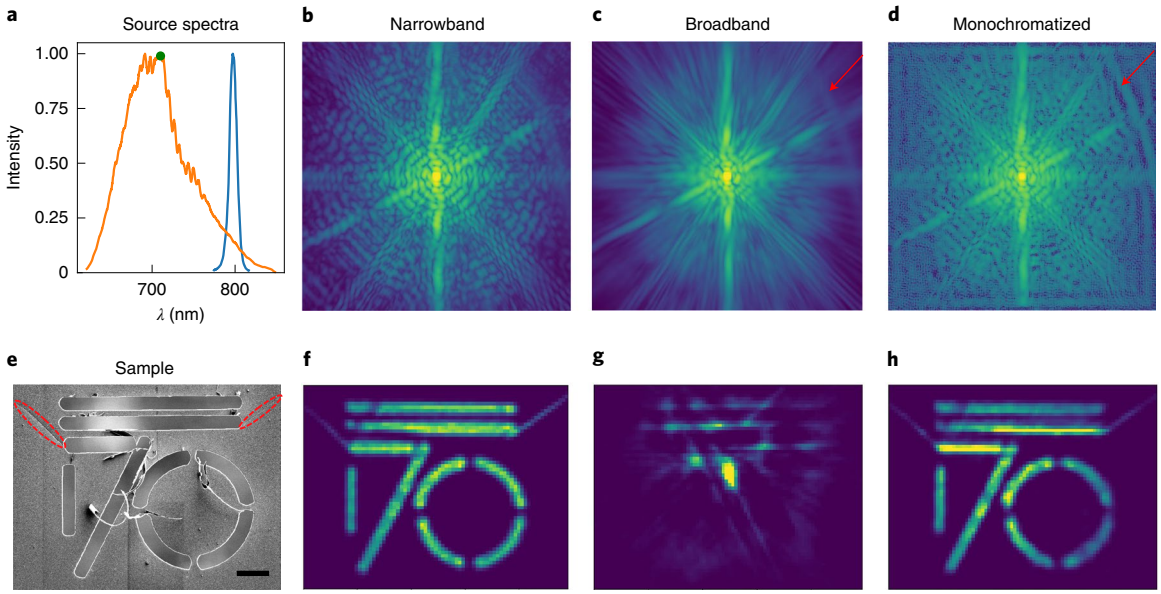

Fig. 2 | Experimental validation in the visible spectrum. a, The broadband spectrum (orange) with a bandwidth of $\Delta\lambda/\lambda = 11\%$ and the narrowband spectrum (blue) with a bandwidth of $\Delta\lambda/\lambda = 1.2\%$. The green dot at 710 nm represents the central wavelength λ_c, which is taken at the centre of mass of the spectrum. **b**, Narrowband diffraction pattern. **c**, Broadband diffraction pattern. The red arrow indicates a band of stray light, which causes an artefact in the monochromatized pattern. Both patterns contain about 10^{11} photons. **d**, Monochromatized diffraction pattern from the broadband data in **c**. The red arrow indicates an artefact caused by the monochromatization of the band of stray light, which does not follow the spectral convolution expected by the monochromatization method. **e**, SEM image of the sample. Scale bar, 10 μm. Two membrane cracks are indicated by red dashed lines. **f**, Reconstruction for the narrowband case. **g**, CDI reconstruction directly from the broadband pattern in **c**. **h**, Reconstruction of the monochromatized diffraction pattern in **d**. Note how the cracks in the membrane are visible in both successful reconstructions.

is, $\lambda_c = 710$ nm. This allowed the successful recovery of the speckles and of most of the features. The similarity between the narrowband pattern and the monochromatized result (Fig. 2d) is obvious. Some artefacts from the numerical process nevertheless deserve attention, for instance, the band of stray light indicated by the red arrow in the broadband pattern (Fig. 2c). This stray light is not part of the real diffraction pattern and thus does not follow the spectral convolution expected by the inversion method. In the monochromatized pattern the inversion of this stray light causes unphysical oscillations (indicated by the red arrow in Fig. 2d). Another unphysical feature that we systematically find is the squared structure at the edges of the monochromatized pattern. These regions are dominated by noise, which does not follow the expected spectral convolution either. Thanks to the regularized inversion method, these artefacts are not dominant in the monochromatized pattern and do not obstruct the phase retrieval.

The phase retrieval was performed using the diffraction patterns as input into a difference map algorithm[37], with a shrink-wrap-like support update[38] (see Methods). The reconstruction procedure was applied to the three diffraction patterns displayed in Fig. 2b–d. The corresponding retrieved objects are shown in Fig. 2f–h. Whereas the CDI algorithm does not reach convergence when using the broadband diffraction pattern (Fig. 2g) and only some lines are barely retrieved, the sample is readily reconstructed for both the monochromatic (Fig. 2f) and numerically monochromatized cases (Fig. 2h). In the monochromatized reconstruction, most of the features visible in the SEM image are reproduced with high fidelity, even the cracks in the membrane (indicated in red in Fig. 2e). However, the residual sub-micrometre gold wires visible from the patterning are not visible as they scale below the spatial resolution. A more inhomogeneous distribution of the intensity in the monochromatic case is observed, but the high quality of the result validates our approach.

To test the method's sensitivity to noise, the experimental validation was reproduced for signal levels spanning six orders of magnitude. The resolution derived from the $1/e$ criterion on the phase retrieval transfer function (PRTF)[14] is plotted for each signal level in Fig. 3. Our broadband method performs similarly to the narrowband case in the high-signal regime and slightly outperforms the narrowband case in the low-signal regime. A possible explanation for this behaviour could be the noise-suppressing properties of the CGLS regularization method used in the inversion of matrix C (see for example ref. [35]).

From Fig. 3, it seems that the obtained resolution is flat over a signal increase of two orders of magnitude. We can give another estimate of the resolution by looking at the smallest features that have been reconstructed reliably, which are the two oblique cracks in the membrane. They are visible in all high-signal reconstructions and disappear only below a signal level of 10^7 photons. A lineout across these cracks in the reconstruction has a full-width at half-maximum (FWHM) of about 2.5 μm. This estimate thus gives a higher resolution than the theoretical resolution limit of 5.5 μm determined by the coherence length for the general broadband case.

X-ray experiment. To test our method in the hard X-ray regime, we performed a validation experiment at the SOLEIL synchrotron (France) at the Nanoscopium undulator beamline[39]. Synchrotron radiation does not offer a broad spectrum of spatially coherent radiation, so a broadband source was emulated by summing monochromatic diffraction patterns at different energies of the X-ray beam.

The sample chosen for this experiment consisted of a Siemens star resolution target with 10-μm-length spokes and a 20-μm total diameter (see Methods). The sample was illuminated in transmission geometry to collect single diffraction patterns at successive energies, ranging from 7.1 to 8.0 keV in steps of 4 eV. The sum of the patterns yields a broadband diffraction pattern of 12% bandwidth. As shown in Fig. 4a, the pattern displays some characteristics already observed in the experiment in the visible spectrum: it is blurred and it does not present the features that we would expect for

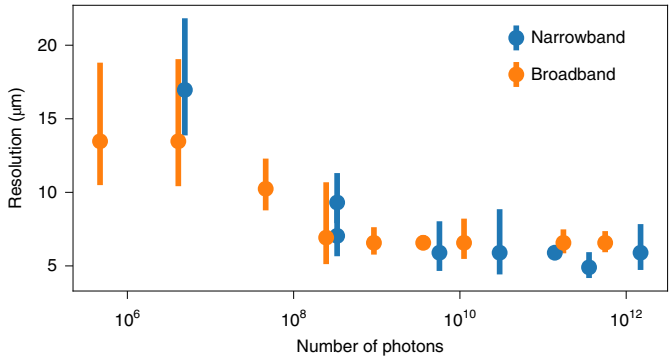

Fig. 3 | Resolution of the reconstructions as a function of the signal level. The resolution of the reconstructions obtained from the 1/*e* criterion on the PRTF is plotted as a function of the total number of photons in the raw measured diffraction patterns. Our broadband method performs similarly to the conventional narrowband case and even better in the low-signal regime. The error bars are determined from the spread of the PRTF (see Methods).

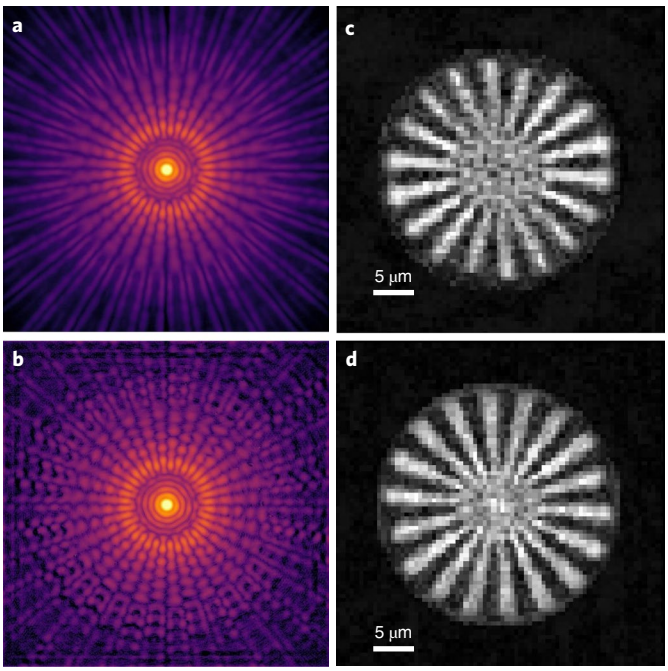

Fig. 4 | X-ray experimental validation using synchrotron radiation. **a**, Broadband diffraction pattern obtained by summing all the acquired monochromatic diffraction patterns. **b**, Diffraction pattern obtained after numerical monochromatization of the diffraction pattern in **a**. **c**, Reconstructed amplitude of the Siemens star sample from the monochromatized broadband diffraction pattern in **b**. **d**, Reconstructed amplitude of the same object from a single monochromatic diffraction pattern.

a coherently illuminated object, such as the frequency modulation of the streaks arising from the star's spokes. Our monochromatization process was then performed on the pattern. The result is shown in Fig. 4b, monochromatized up to $k = 16$ and exhibiting sharp features and interference fringes. The appearance of artefacts near the borders is noticeable.

Phase retrieval was then performed using the PyNX[40] package (see Methods). Figure 4c shows the reconstructed magnitude of the sample from the broadband pattern after monochromatization. For comparison, the same phase retrieval procedure was applied to a single monochromatic diffraction pattern (at 7.1 keV), shown in Fig. 4d. It should be noted that the reconstructed pixel size is 560 nm owing to the experimental configuration, which is why the smallest features of the test sample are not reconstructed. However, this proof-of-principle experiment did not aim to resolve the internal sub-micrometre features of the Siemens star. Overall, the quality and the resolution of the broadband reconstruction are lower than that of the monochromatic benchmark, which is attributed to instabilities when successively acquiring the monochromatic diffraction patterns.

Discussion

We have demonstrated successful image reconstruction from only one broadband coherent diffraction pattern, paving the way towards single-shot attosecond lensless imaging. Our method is based on the numerical monochromatization of the broadband diffraction pattern through the regularized inversion of the matrix-vector problem. This method is a standalone step before the application of the phase retrieval algorithm and depends only on the spectrum of the diffracted radiation. The method has been tested to be robust at low signal levels. We have successfully validated our method experimentally with more than 10% bandwidth and up to the hard X-ray photon energy range. This applicability can be expanded to several tens of per cent bandwidth (depending on experimental parameters; see Extended Data Fig. 2 and Supplementary Information). The method can be applied to any technique based on coherent elastic scattering of any type of coherent radiation. Furthermore, since our technique is applied as a step before the phase retrieval process itself, both single-shot CDI and ptychography could benefit from it. The possibility of using broadband illumination in lensless imaging demonstrated here will open up a wide range of opportunities in attosecond science. Attosecond nanoscale flash imaging is now potentially accessible at a number of HHG facilities. Attosecond X-ray free-electron lasers and other broadband X-ray sources such as inverse Compton scattering sources[41,42] are being built and can benefit from our method. The two-step aspect (monochromatization followed by phase retrieval) of the method allows a fast flow of the data that can be of benefit, for example, in real-time functional imaging in the semiconductor industry (see refs. [36,43] and Supplementary Information). Because of its generality the method can also be applied to various problems in modern optics, such as aberration correction.

Online content

Any methods, additional references, Nature Research reporting summaries, source data, extended data, supplementary information, acknowledgements, peer review information; details of author contributions and competing interests; and statements of data and code availability are available at https://doi.org/10.1038/s41566-020-0660-7.

Received: 2 September 2019; Accepted: 9 June 2020;
Published online: 20 July 2020

References

1. Krausz, F. & Ivanov, M. Attosecond physics. *Rev. Mod. Phys.* **81**, 163–234 (2009).
2. Galmann, L., Cirelli, C. & Keller, U. Attosecond science: recent highlights and future trends. *Annu. Rev. Phys. Chem.* **63**, 447–469 (2012).
3. Calegari, F., Sansone, G., Stagira, S., Vozzi, C. & Nisoli, M. Advances in attosecond science. *J. Phys. B* **49**, 062001 (2016).
4. Lindroth, E. et al. Challenges and opportunities in attosecond and XFEL science. *Nat. Rev. Phys.* **1**, 107–111 (2019).
5. Takahashi, E. J., Lan, P. & Midorikawa, K. Generation of an isolated attosecond pulse with microjoule-level energy. In *Conference on Lasers and Electro-Optics* Paper QTh5B.10 (OSA, 2012).
6. Chapman, H. N. et al. Femtosecond diffractive imaging with a soft-X-ray free-electron laser. *Nat. Phys.* **2**, 839–843 (2006).
7. Ravasio, A. et al. Single-shot diffractive imaging with a table-top femtosecond soft X-ray laser-harmonics source. *Phys. Rev. Lett.* **103**, 028104 (2009).

8. Teichmann, S. M., Silva, F., Cousin, S. L., Hemmer, M. & Biegert, J. 0.5-keV soft X-ray attosecond continua. *Nat. Commun.* **7**, 11493 (2016).
9. Popmintchev, T. et al. Bright coherent ultrahigh harmonics in the keV X-ray regime from mid-infrared femtosecond lasers. *Science* **336**, 1287–1291 (2012).
10. Ding, Y., Huang, Z., Ratner, D., Bucksbaum, P. & Merdji, H. Generation of attosecond x-ray pulses with a multicycle two-color enhanced self-amplified spontaneous emission scheme. *Phys. Rev. Spec. Top. Accel. Beams* **22**, 060703 (2009).
11. Hartmann, N. et al. Attosecond time–energy structure of X-ray free-electron laser pulses. *Nat. Photon.* **12**, 215–220 (2018).
12. Gorkhover, T. et al. Femtosecond and nanometre visualization of structural dynamics in superheated nanoparticles. *Nat. Photon.* **10**, 93–97 (2016).
13. Miao, J. W., Charalambous, P., Kirz, J. & Sayre, D. Extending the methodology of X-ray crystallography to allow imaging of micrometre-sized non-crystalline specimens. *Nature* **400**, 342–344 (1999).
14. Chapman, H. N. et al. High-resolution ab initio three-dimensional x-ray diffraction microscopy. *J. Opt. Soc. Am. A* **23**, 1179–1200 (2006).
15. Nishino, Y., Takahashi, Y., Imamoto, N., Ishikawa, T. & Maeshima, K. Three-dimensional visualization of a human chromosome using coherent X-ray diffraction. *Phys. Rev. Lett.* **102**, 018101 (2009).
16. Chapman, H. N. & Nugent, K. A. Coherent lensless X-ray imaging. *Nat. Photon.* **4**, 833–839 (2010).
17. Ekeberg, T. et al. Three-dimensional reconstruction of the giant mimivirus particle with an x-ray free-electron laser. *Phys. Rev. Lett.* **114**, 098102 (2015).
18. Miao, J., Ishikawa, T., Robinson, I. K. & Murnane, M. M. Beyond crystallography: diffractive imaging using coherent x-ray light sources. *Science* **348**, 530–535 (2015).
19. Duarte, J. et al. Computed stereo lensless X-ray imaging. *Nat. Photon.* **13**, 449–453 (2019).
20. Fienup, J. R. Phase retrieval for undersampled broadband images. *J. Opt. Soc. Am. A* **16**, 1831–1837 (1999).
21. Williams, G. O. et al. Fourier transform holography with high harmonic spectra for attosecond imaging applications. *Opt. Lett.* **40**, 3205–3208 (2015).
22. Gonzalez, A. I. *Single Shot Lensless Imaging with Coherence and Wavefront Characterization of Harmonic and FEL sources*. PhD thesis, Université Paris-Saclay (2016).
23. Witte, S., Tenner, V. T., Noom, D. W. & Eikema, K. S. Lensless diffractive imaging with ultra-broadband table-top sources: from infrared to extreme-ultraviolet wavelengths. *Light Sci. Appl.* **3**, e163 (2014).
24. Meng, Y. et al. Octave-spanning hyperspectral coherent diffractive imaging in the extreme ultraviolet range. *Opt. Express* **23**, 28960–28969 (2015).
25. Batey, D. J., Claus, D. & Rodenburg, J. M. Information multiplexing in ptychography. *Ultramicroscopy* **138**, 13–21 (2014).
26. Enders, B. et al. Ptychography with broad-bandwidth radiation. *Appl. Phys. Lett.* **104**, 171104 (2014).
27. Enders, B. & Thibault, P. A computational framework for ptychographic reconstructions. *Proc. R. Soc. Lond. A* **472**, 20160640 (2016).
28. Gerchberg, B. R. W. & Saxton, W. O. A practical algorithm for the determination of phase from image and diffraction plane pictures. *Optik* **35**, 237–246 (1972).
29. Abbey, B. et al. Lensless imaging using broadband X-ray sources. *Nat. Photon.* **5**, 420–424 (2011).
30. Dilanian, R. A. et al. Diffractive imaging using a polychromatic high-harmonic generation soft-x-ray source. *J. Appl. Phys.* **106**, 023110 (2009).
31. Chen, B. et al. Multiple wavelength diffractive imaging. *Phys. Rev. A* **79**, 023809 (2009).
32. Teichmann, S., Chen, B., Dilanian, R. A., Hannaford, P. & Van Dao, L. Experimental aspects of multiharmonic-order coherent diffractive imaging. *J. Appl. Phys.* **108**, 023106 (2010).
33. Chen, B. et al. Diffraction imaging: the limits of partial coherence. *Phys. Rev. B* **86**, 235401 (2012).
34. Paganin, D. *Coherent X-Ray Optics* (Oxford University Press, 2007).
35. Hansen, P. C. REGULARIZATION TOOLS: A matlab package for analysis and solution of discrete ill-posed problems. *Numerical Algorithms* **6**, 1–35 (1994).
36. Huijts, J. *Broadband Coherent X-ray Diffractive Imaging and Developments Towards a High Repetition Rate Mid-IR Driven keV High Harmonic Source*. PhD thesis, Université Paris-Saclay (2019).
37. Elser, V., Rankenburg, I. & Thibault, P. Searching with iterated maps. *Proc. Natl Acad. Sci. USA* **104**, 418–423 (2007).
38. Marchesini, S. A unified evaluation of iterative projection algorithms for phase retrieval. *Rev. Sci. Instrum.* **78**, 011301 (2007).
39. Somogyi, A. et al. Optical design and multi-length-scale scanning spectro-microscopy possibilities at the Nanoscopium beamline of Synchrotron Soleil. *J. Synchrot. Radiat.* **22**, 1118–1129 (2015).
40. Mandula, O., Elzo Aizarna, M., Eymery, J., Burghammer, M. & Favre-Nicolin, V. *PyNX.Ptycho*: a computing library for X-ray coherent diffraction imaging of nanostructures. *J. Appl. Crystallogr.* **49**, 1842–1848 (2016).
41. Variola, A., Haissinski, J., Loulergue, A. & Zomer, F. (eds) *ThomX Technical Design Report* (2014); http://hal.in2p3.fr/in2p3-00971281
42. Günther, B. et al. The Munich Compact Light Source: biomedical research at a laboratory-scale inverse-Compton synchrotron X-ray source. *Microsc. Microanal.* **24**, 984–985 (2018).
43. Zhang, B. et al. Full field tabletop EUV coherent diffractive imaging in a transmission geometry. *Opt. Express* **21**, 21970–21980 (2013).

Publisher's note Springer Nature remains neutral with regard to jurisdictional claims in published maps and institutional affiliations.

© The Author(s), under exclusive licence to Springer Nature Limited 2020

Methods

Numerical implementation. The matrix C is fully determined by the spectrum and the size of the diffraction pattern. Defining the scaling factor $\alpha = \lambda/\lambda_c$, in one dimension C is formed as follows:

$$C_{nj} = \sum_L \underbrace{[\min\{j, \alpha_l n\} - \max\{j-1, \alpha_l(n-1)\}]}_{\text{part of scaled pixel } n \text{ falling onto pixel } j} \frac{S_l}{\alpha_l} \tag{5}$$

where

$$N = \left\{n : \frac{j-1}{\alpha_{max}} < n < \frac{j}{\alpha_{\min}+1}\right\},$$
$$L = \left\{l : \frac{j-1}{n} < \alpha_l < \frac{j}{n-1}\right\}.$$

Here l, n, j are the indices that run over α, **m**, **b**, respectively, and S_l is the spectral weight for scaled pattern l. This expression can be understood as the contribution of pixel n of **m** to pixel j of **b** is given by the part of pixel n that falls onto pixel j for the scaled pattern l times the spectral weight, summed over all L. Extended Data Fig. 1 depicts the information flow in our method.

In the experiment the broadband pattern and the spectrum are measured (this is either a corrected source spectrum or the spectrum of the diffracted radiation, and both should be corrected for the response of the camera). The measured pattern was centred and binned to obtain pattern **B**. The spectrum was normalized to obtain $S(\alpha)$, which, combined with the size of **B**, is all the information that is needed to compute matrix C. In our experimental validation in the visible spectrum, **B** was 480 × 480 pixels. This means that C had 240^4 values (the scaling was the same for each quadrant). Luckily, C is a sparse matrix, depending on the spectrum only a few per cent of the values are non-zero. C was built by evaluating equation (5) in a set of parallel for-loops running only over the non-zero part of C. Note that C only has to be built once per spectrum (and size of **B**). As C is highly ill-conditioned, inversion of the problem is performed using a regularization method called CGLS (see for example ref. [35]). It consists of minimizing the least-squares problem

$$\min_x \| Cx - b\|_2 \qquad \text{subject to} \quad x \in \mathcal{K}_k \tag{6}$$

where $\mathcal{K}$ denotes the so-called Krylov subspace:

$$\mathcal{K}_k \equiv \text{span}\{C^{\mathrm{T}}b, C^{\mathrm{T}}CC^{\mathrm{T}}b, \ldots, (C^{\mathrm{T}}C)^{k-1}C^{\mathrm{T}}b\}. \tag{7}$$

The power of this method is its behaviour of semi-convergence: for increasing k, first the signal is inverted so x comes close to the exact solution, then the noise starts being inverted as well and x diverges (see refs. [35,36] and Supplementary Videos 1 and 2). Typically, the inverted patterns M'_k are computed up to $k_{\max} = 40$, M'_k is then visually inspected and the optimum value for k is chosen (typically $k_{\text{opt}} \approx 25$, depending on the signal-to-noise ratio). For the experiment in the visible spectrum, k_{opt} was chosen manually, for the X-ray data a cross-correlation method was used. This process can also be performed completely automatically by performing phase retrieval for different values of k and selecting the most reliable reconstruction. The monochromatized pattern $M'_{k_{\text{opt}}}$ now serves as the input for a conventional phase retrieval algorithm. The numerical implementation was based on a Matlab function[35] that was translated to Python with the addition of two constraints: positivity of x_k (photon counts should not be negative) and a support constraint on the Fourier transform of x_k. The latter is justified as we are dealing with isolated samples (the typical constraint for CDI), so the sample's autocorrelation is isolated as well. These constraints help to further improve the regularizing power of the method.

Experiments and data analysis. *Optical experiment.* Repetition of the experiment proved excellent stability of the supercontinuum source. An off-axis parabola with an effective focal length of 75 mm was used to focus the beam on the sample, which was mounted on a translation stage. The sample consisted of a gold-coated silicon nitride membrane in which an aperture was etched using a focused ion beam. A CCD camera (Illunis RMV 4022) was used to acquire the diffraction pattern, at a distance of 16 mm from the sample. This corresponds to a numerical aperture of 0.39 for the diffraction patterns shown in Fig. 2. High-quality diffraction patterns were routinely obtained, attesting excellent robustness and stability of the supercontinuum source properties such as coherence, amplitude and beam pointing. These patterns were constructed by combining high-dynamic-range acquisitions at different neutral density filters, such that the effective bit-depth of the shown images is up to 24. They subsequently underwent three pre-processing steps of a 3 × 3 binning yielding patterns of 480 × 480 pixels, numerical monochromatization (broadband case only) and erosion outside a user-selected mask (noise suppression). The sample was then reconstructed using a difference map algorithm with a shrink-wrap-like support, within a maximum of 1,000 iterations. 1,024 independent reconstructions were launched with random starting points to compute the PRTF. The successful reconstructions were then user-selected to be registered (using an adaptation from ref. [44]) and averaged to enhance the signal on the final result. To compute the error bars in Fig. 3, the 1,024 independent reconstructions were divided in 8 subgroups of 128 reconstructions. The spatial frequency q for which the PRTF falls below $1/e$ was then determined for each subgroup and the standard deviation of these 8 values was taken as the error on q. The plotted resolution is $1/q$, which is why the error in the real-space resolution is asymmetric.

Synchrotron experiment. Nanoscopium is an undulator beamline that, with a distance of about 150 m between the undulator and the experimental hutch, has been developed specifically for applications requiring excellent spatial coherence[39]. In our experiment, monochromatic X-rays (starting at 7.1 keV) entered the experimental hutch. The coherent part of the beam was selected by an aperture, consisting of a pair of slits set to 1 × 1 mm^2. After, the X-ray beam passes through a tungsten pinhole of 24 μm diameter and hits the sample. The Siemens star gold test pattern consisted of 18 spokes fabricated by electron-beam lithography and gold electroplating on a 500-nm-thick silicon nitride membrane. The detector used to record the diffracted signal was an indirect imaging device based on a 70-μm-thick LuAG:Ce scintillator coupled with a scintillator to magnify the image onto a large, fast and sensitive CMOS camera (Hamamatsu ORCA Flash 4.0 sCMOS). It was placed 331 cm from the sample. The field of view covers 1.3 mm side and the measured spatial resolution is about 2 μm (FWHM). A microscope objective of ×5 magnification was used for preliminary alignment, allowing to locate the sample under the beam.

The X-ray intensity was first monitored using an 8-μm-thick silicon diode, the X-ray energy was measured through the X-ray fluorescence spectra acquired by a silicon drift detector. Diffraction patterns were acquired using a high dynamic range: each pattern consisted of a long (10 s) and a short (1 s) acquisition. The long acquisition contains information at high scattering angles, the information at the saturated centre of the camera is obtained from the short acquisition (with a multiplicative factor of 10). As the X-ray energy needed to be scanned over a long range the undulator separation and monochromator position needed to be varied. Special attention was paid to the stability of the undulator and monochromator during the scan to avoid artefacts in the broadband diffraction pattern due to a possible shift of the beam on the sample.

The phase retrieval of the synchrotron data was performed using the Python library PyNX[40] (http://ftp.esrf.fr/pub/scisoft/PyNX/doc/). The initial support was chosen to be a circle and the convergence was achieved after 32 iterations of a sequence of 20 error reduction (ER)[28] and 50 hybrid input–output (HIO)[45] algorithms. The images shown in Fig. 4c,d are the raw reconstructions, meaning that no post-treatment was performed on them. In this way, monochromatic and monochromatized reconstructions are comparable.

Data availability

The data that support the plots within this paper and other findings of this study are available from the corresponding author upon reasonable request. Source data are provided with this paper.

Code availability

The developed Python code is available at https://github.com/jhuijts under the BSD license.

References

44. Guizar-Sicairos, M., Thurman, S. T. & Fienup, J. R. Efficient subpixel image registration algorithms. *Opt. Lett.* **33**, 156–158 (2008).
45. Fienup, J. R. Reconstruction of an object from the modulus of its Fourier transform. *Opt. Lett.* **3**, 27–29 (1978).

Acknowledgements

We acknowledge financial support from the European Union through the Future and Emerging Technologies (FET) Open H2020: VOXEL (grant 665207) and PETACom (grant 829153) and the integrated initiative of European laser research infrastructure (LASERLAB-EUROPE) (grant agreement no. 654148). Support from the French ministry of research through the 2013 Agence Nationale de Recherche (ANR) grants 'NanoImagine', 2014 'ultrafast lensless Imaging with Plasmonic Enhanced Xuv generation (IPEX)', 2016 'High rEpetition rate Laser for Lensless Imaging in the Xuv (HELLIX)'; from the DGA RAPID grant 'SWIM', from the Centre National de Compétences en Nanosciences (C'NANO) research programme through the NanoscopiX grant; the LABoratoire d'EXcelence Physique Atoms Lumiére Matiére—LABEX PALM (ANR-10-LABX-0039-PALM), through the grants 'Plasmon-X' and 'HIgh repetition rate Laser hArmonics in Crystals (HILAC)' and, finally, the Action de Soutien á la Technologie et á la Recherche en Essonne (ASTRE) programme through the 'NanoLight' grant are also acknowledged. We would like to acknowledge the support of F. Fortuna and L. Delbsq from CSNSM, IN2P3, Orsay for sample fabrication. We aknowledge M. Hanna (LCF, IOGS Palaiseau), F. Guichard (Amplitude Techologies), M. Natile (Amplitude Techologies) and Y. Zaouter (Amplitude Techologies) for support during the experimental validation of the method in the visible spectrum. We aknowledge G. Dovillaire and S. Bucourt (Imagine Optic, Orsay, France) for providing the CCD camera. We also appreciate discussions with T. Auguste, F. Maia, H. Chapman, L. Shi, M. Kovacev and B. Daurer on the principle and implementation of the method and acknowledge access to the Davinci computer

cluster of the Laboratory of Molecular Biophysics (Uppsala University, Sweden) and support by M. Hantke on the use of Condor. Contributions to the detector development from K. Desjardins from SOLEIL (Saint Aubin, France) were crucial to the success of the synchrotron experiment.

Author contributions

J.H. and H.M. proposed the physical concept. J.H. developed the monochromatization method and performed the experiment in the visible spectrum, H.M. and J.H. devised the experiments, all authors performed the X-ray demonstration. Monochromatization of the synchrotron data was performed by J.H., phase retrieval by S.F. All authors discussed the results and contributed to writing the manuscript.

Competing interests

The authors declare no competing interests

Additional information

Extended data is available for this paper at https://doi.org/10.1038/s41566-020-0660-7.

Supplementary information is available for this paper at https://doi.org/10.1038/s41566-020-0660-7.

Correspondence and requests for materials should be addressed to H.M.

Reprints and permissions information is available at www.nature.com/reprints.

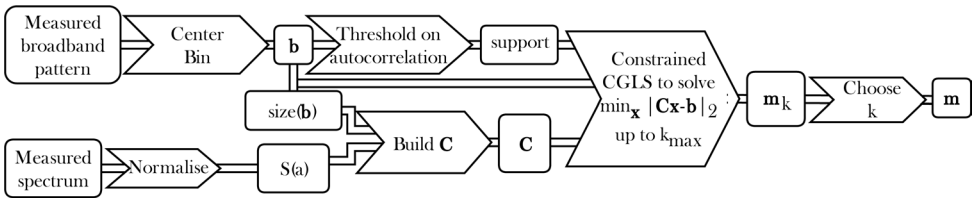

Extended Data Fig. 1 | Information flowchart of our method. Based solely on the measured broadband diffraction pattern and the measured spectrum of the diffracted radiation, the broadband diffraction pattern (**b**) is monochromatised (yielding **m**). **C** is the matrix containing the spectral information, CGLS stands for Conjugate Gradient Least Squares, the regularisation method used to minimize the amount of inverted noise (see Methods).

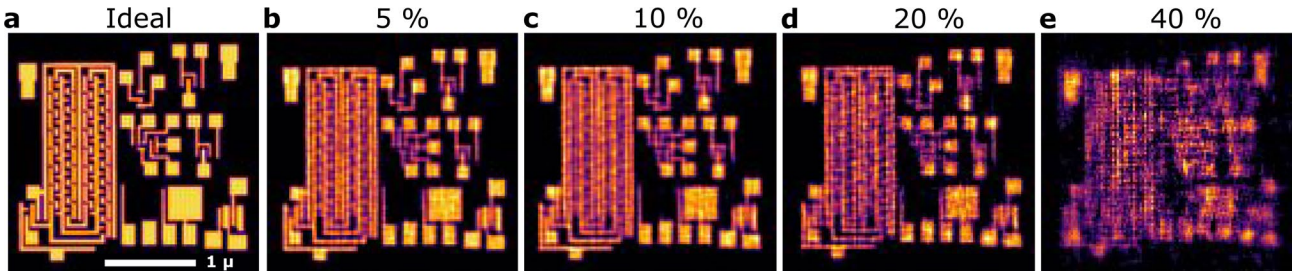

Extended Data Fig. 2 | Pushing the bandwidth in a broadband X-ray CDI simulation. The ideal reconstruction a and reconstructions for 5 to 40% bandwidth **b**–**e** at a signal level of 10^{14} photons in the broadband pattern.